IUST
Iran University of Science and Technology

Iranian Journal of Electrical and Electronic Engineering

Journal Homepage: ijeee.iust.ac.ir

Research Paper

A Study of the Linear Electromagnetic Generator for Harvesting Electrical Energy from Initial Acceleration: Design, Optimization, and Experimental Validation

A. Rajabi* and H. Lexian*(C.A.)

Abstract: One of the important requirements in projectiles is to design a power supply for fuse consumption. In this study, an optimum design for the power supply, which includes a Miniaturized Inertia Generator (MIG), was introduced. The main objective of this research was to optimize the dimensions of the MIG with the aim of increasing energy. To achieve this, the design of experiment (DOE) was carried out through RSM-BBD to optimize six parts of the MIG. Numerical simulations were performed using Maxwell's software. After analyzing of results by ANOVA and extracting the optimum result from the RSM, a Miniaturized Inertia Generator was fabricated with optimum dimensions. The results showed that the MIG with optimum dimensions at an acceleration of 800'g could generate 15.25V and stores the generated energy using an RLC circuit within 1ms. The experimental results which were obtained by the shock test system showed that 14.75V was charged on a capacitor within 1.1ms which has good conformity with the numerical results. The results indicated that the proposed design not only increased the MIG efficiency, but also determined the effect of each parameter on the produced energy and efficiency.

Keywords: Design Optimization, Linear Electromagnetic Generator, Energy Harvesting, Safety Mechanism, FEM, Power Supply.

1 Introduction

IN many applications, including projectiles, a miniaturized electromechanical system must be completely integrated inside the system without any physical connection with the external environment, that it should include a power supply. A typical solution for a power supply is the use of a battery, but batteries are unsuitable for reasons such as the storage limit in the store, energy limitation, large volume, toxicity, and chemical content. So an alternative to batteries can be a source of renewable energy. Renewable-energy sources can convert energy from an environment source to the electrical energy [1], which, depending upon the application, can use chemical, mechanical, thermal and light energy [2].

A solar cell [3], although so far three generations have been produced [4-8] and have characteristics such as; the possibility of manufacturing in micro dimensions, long life and output power of about 5-30mW/cm^2 [9] but there are disadvantages like the restriction of use in rain or night. The production of electrical energy from thermal energy, first discovered by Thomas Seebeck [10] and then developed [11], has the following characteristics: direct conversion of energy, lack of using moving parts, no noise and low volume [12]. However, the low output power of 0.01-0.1 mW/cm^2 is one of the disadvantages [9] which was also tested in the projectiles [13]. The production of electrical energy from chemical processes may occur with combustion [14] or high inertia acceleration [15]. In the combustion process, although high power is produced but due to the limited size of small projectiles, there is not the possibility of using them. The process of high inertia acceleration can be used in small size, but low energy density and its dilatory activation are among its disadvantages. The energy harvesting from mechanical

Iranian Journal of Electrical and Electronic Engineering, 2021.
Paper first received 02 May 2019, revised 26 December 2019, and accepted 30 December 2019.
* The authors are with the Faculty of Material & Manufacturing Technologies, Malek Ashtar University of Technology (MUT), Tehran, Iran.
E-mails: amirhossein.rajabi1992@yahoo.com and lexian@mut.ac.ir.
Corresponding Author: H. Lexian.
https://doi.org/10.22068/IJEEE.17.1.1490

motion is another form of electrical energy production, with the maximum output power of 10-100mW/cm^2 [9] that is including electrostatic induction, piezoelectric, Triboelectric and electromagnetic induction. An electrostatic induction generator, although lightweight, but has some disadvantages, such as the need for initial charging for setting up and low-current. The piezoelectric generator, like electrostatic induction, has low efficiency, in addition to disadvantages such as high-output impedance. Triboelectric generator, unlike the above two generators, has high power and efficiency and can be manufactured in nano-dimensions, whereas like mention generators, there is a high-output impedance that delays the use of its output in the projectile [16-18]. Among different generators, generators based on mechanical motion and electromagnetic induction, not only have the advantages such as high-output current, low impedance, the feasibility of manufacturing in micro-sized, but also they provide high efficiency and the possibility of using the produced energy in the shortest possible time. Therefore, they can be used in small-caliber projectiles [9]. These generators are known as Basel's generators [19].

These generators are activated by initial acceleration. When the generator is under accelerating, core, including the magnet and iron disc, is moved into the housing and completes the magnetic flux loop around the wire. According to Faraday's induction law, this displacement produces a voltage. In this generator, a shear plate is considered, that due to safety, it cut off in a certain range of acceleration. So far, various investigations have been carried out on these generators, which are briefly discussed follow. Wang *et al*. [20] developed a 2-phase inertia generator. This model was designed with structurally different from the Basel's model. Optimization with finding the optimum ratio between parameters a generator was done. The results showed with increasing speed from 0.15 to 0.45m/s, The voltage and energy changed from 12 to 16.5V and 2.45 to 6.63mJ respectively. It also caused the capacitor to charge faster. Based on the above mechanism, Fu *et al*. [21] used a novel nanomagnetic material. The material name of the novel nanomagnetic was 90ω/ %Ne14 Fe79.5 Ga0.5 B6 and 10ω/ %Ne6 Fe87 Nb1 B6, which produced 23.5V under an 8000'g acceleration whereas a typical magnetic material with same conditions generated 16.75V. The results showed that a 40% increase in the produced voltage was caused by using nanomagnetic material. In order to increase the voltage and efficiency, Fark *et al*. [22] provided an optimum model to extract energy from ocean waves by Inertia generators. This optimum model is a new mathematical model based on the genetic algorithm. This model by optimizing the shape of any Inertia generator achieves multiple goals such as maximizing power generation and generating a smaller generator. Also, Lu *et al*. [23] done experiments with the various topologies of the permanent magnet to observe the effect of magnets charging on the generator voltage. In this study, the magnetization direction of magnets is divided into two types such as radial and axial. After testing, magnets generated more energy with axial charge, although they were discharged sooner. Furthermore, Yoon *et al*. [24] introduced a simpler design that consisted of a ring magnet and a metal bobbin. The design, which is presented with two prototypes, showed that one of these generators with miniaturized dimensions under the 30,000'g acceleration, stored 15V in the 30μF capacitor within 0.07ms. Although, the sample has a simple design, but due to the displacement of the magnet and the formation of an open magnetic circuit, that part of the circuit is air with high reluctance; therefore, the magnetic flux rate decreases. On the other hand, the Basel's generator possesses a magnetic closed circuit during the process, and higher permeability of iron and magnet relative to the air caused increasing the magnetic flux rate. So it was chosen for optimizing.

Due to the importance of Restriction the dimensions of miniaturized power supplies and increasing the produced energy of these resources, their optimization is important. In practice because of the multiplicity of parameters and time-consuming of each new design using Maxwell's software, conventional optimization algorithms such as genetic algorithms cannot be used. Therefore, in this research, optimization using RSM-BBD was carried out based on flowcharts Fig. 1. This optimization was performed on six parameters of the MIG who is described in the methodology section. The six parameters of the MIG are core diameter, magnet height, housing height, disc height, wall thickness of housing and thickness of the housing lid. After extracting the optimum dimensions of the MIG, the effect of each parameter was determined on the energy. Finally, the verification was performed with the shock test system according to Fig. 2.

2 Methodology

RSM is one of the optimization methods that are widely used to obtain the optimum model of an output that is the function of the multiple input variables. In this research, Box-Behnken design (BBD) with a regression model has been used to find the optimum dimension of the six parameters, which is designed in three levels. Parameters were considered as the MIG parts. The MIG can generate electrical energy from the initial acceleration of the projectiles.

2.1 MIG Parameters

Due to the numerous parts used in the MIG and also the space limitation of the MIG in a particular application, six parameters that are parts of the MIG, were selected for dimensions optimization. These parameters include core diameter, magnet height,

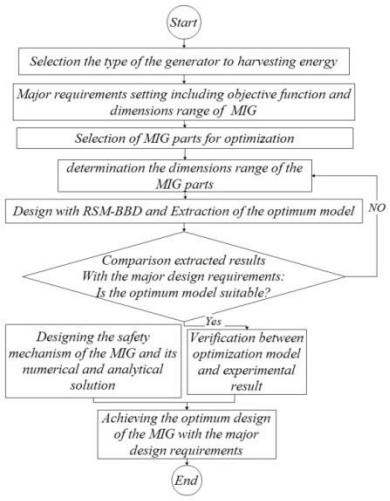

Fig. 1 MIG optimization flowchart.

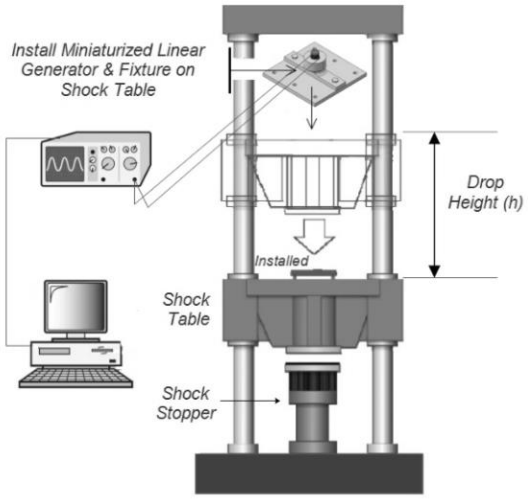

Fig. 2 The structure of the shock test system.

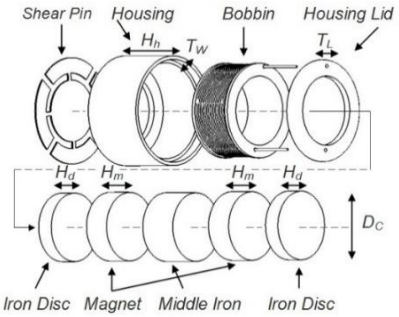

Fig. 3 Graphic representation of the MIG parameters.

Table 1 Levels considered for each parameter.

Independent variable	Unit	Symbols	Range and level		
			-1	0	+1
Core diameter	mm	D_c	6	8	10
Magnet height	mm	H_m	2	3	4
Disc height	mm	H_d	1.5	2	2.5
Housing height	mm	H_h	9	10.5	12
Housing lid thickness	mm	T_L	0.5	1	1.5
Housing thickness	mm	T_W	0.5	1	1.5

housing height, disc height, the wall thickness of the housing and thickness of the housing lid, as shown in Fig. 3.

Each of the parameters mentioned with three levels and the corresponding symbols for optimizes with RSM is listed in Table 1. Fig. 3 also shows these parameters.

The purpose of designing MIG is to supply electrical energy to circuits or sensors of a projectile during time flying. Due to the dimensions limitation of the projectile fuse structure that the MIG is also a part of this; therefore, the dimensions limitation on the MIG is established. With the above-mentioned conditions, in this study, the maximum height of the MIG is 18 mm and the diameter is 16 mm, which were considered at various levels of the six parameters (Table 1).

2.2 Objective Function

Due to the fuse requirement to 10V for the energy supply of the electrical circuit, the optimum output must be in the dimensions' range and produced the mentioned amount minimum. Produced voltage storage must happen quickly, so the electric current parameter also is important. Therefore, the dimensions' optimum output of the MIG should satisfy the condition. Generate at least 10V with the current highest rate. That is why the energy parameter was selected as the objective function.

2.3 Optimum Design Using BBD-RSM

In this research, Box-Behnken design (BBD) was used for optimum design. With regard to the existence of the six-parameters as the input variable for optimization, each of the parameters has three levels; overall, 54 proposals were used in BBD. These 54 proposals are listed in Table 2-I.

2.4 Surface Response Methodology (RSM)

In the RSM, using regression analysis, Information extracted from BBD fit with a quadratic polynomial model. Also, a second-order polynomial equation for each response, through (1) is obtained.

$$Y = \beta_0 + \sum \beta_i X_i + \sum \beta_{ii} X_i^2 + \sum\sum \beta_{ij} X_i X_j + \varepsilon \qquad (1)$$

where Y is the corresponding response, β_0 is a constant sentence, β_i, β_{ii}, β_{ij} are the coefficient of inertia, square and cross-product terms, respectively. Furthermore, the value of ϵ is the error value.

2.5 Modeling MIG

Maxwell 3D software was used to simulate the electromagnetic fields that the MIG model was designed in the transient dynamic workbench. The core of this

MIG consists of five parts attached together, which is moved into the housing by the indirect acceleration of 800'g. To apply the acceleration to the core, at first; the core was defined in a motion-band (Fig. 4(a)), then the acceleration was applied to the motion-band. This acceleration not only causes the core to move but also, by moving the core, a loop of magnetic flux around the coil, to be created (Fig. 4(b)). The excitation module was used to define the winding. At first, the voltage excitation was selected, then the inductance and resistance values and the number of windings were defined. In the mesh module, the MIG parts were meshed. The meshing model is shown in Fig. 4(c), and analysis was done at 2ms.

The parts like the housing, the housing lid and the three metal parts of the core, were all selected from low-carbon steel. They can create a loop of magnetic flux with zero-total vectors during the process through the pass of magnetic flux from themselves. Furthermore, the magnet was chosen from Neodymium (Fe-Ni-B) grade 35, and a layer of nickel was placed on the neodymium magnet to prevent from fast oxidation. The material of the wire and bobbin was selected copper and plastic, respectively; In order to prevent passing flux through the bobbin.

2.6 Electrical Circuit of MIG

Due to the generated voltage through the MIG and its oscillation, as shown in Fig. 5, it can be assumed that:

$$V_s = V_0 \sin(\omega t) \tag{2}$$

where V_0 is the amplitude of the produced voltage and also, ω is the generated voltage frequency by the core movement. It is necessary to store the electrical voltage generated through a circuit in a capacitor with the specified capacity. Capacitor capacitance is calculated by (3), where E is the produced energy in [Joule], V is the produced voltage in [Volt] and also C is the capacitance in [Farad].

$$E = \frac{1}{2}CV^2 \quad \Rightarrow \quad C = \frac{2E}{V^2} \tag{3}$$

Due to the generation of a sinusoidal voltage by the MIG and the need for positive half-wave storage this signal, the governing equations are divided into two half-wave of the sinusoidal. The first part is related to the storage of the positive signal part, and its range is from the beginning of the process to half the period of the signal.

$$\text{First}: \ 0 \le t \le \frac{\pi}{\omega} \tag{4}$$

By applying the second-Kirchoff law for the left mesh Fig. 5, can be written:

$$L_g \dot{I}_{1P} + R_g I_{1P} + \frac{1}{C}\int I_{1P} dt = V_0 \sin(\omega t) \Rightarrow \tag{5}$$

By applying the change of the variable (6), Eq. (5) became the form (7):

$$I_{1P} = +\frac{dQ_{1P}}{dt} \tag{6}$$

$$L\frac{d^2Q_{1P}}{dt^2} + R\frac{dQ_{1P}}{dt} + \frac{Q_{1P}}{C} = V_0 \sin(\omega t) \Rightarrow \tag{7}$$

Given the inhomogeneous of (7), the equation has two

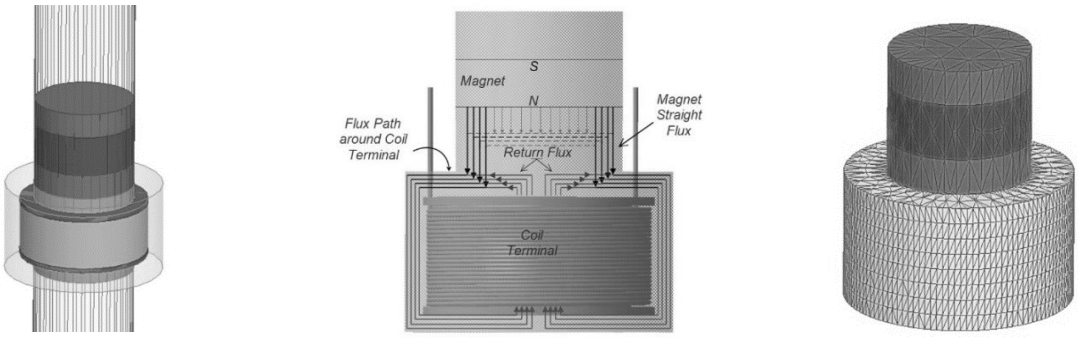

(a) (b) (c)

Fig. 4 a) Modeling of MIG in Maxwell, b) Path of magnetic flux in 2D mode, and c) The meshing model in mesh module.

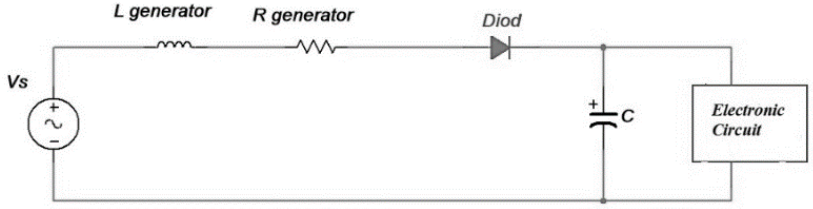

Fig. 5 Electrical circuit of the MIG.

general and private responses for solving the problem. The change of the variable (8) was considered for the private response of the equation.

$$Q_{1P}(t) = Q_0 e^{i(\omega t-\varphi)} \tag{8}$$

Assuming $\alpha = \frac{R}{2L}$, $\omega_0 = \frac{1}{\sqrt{LC}}$, after placing the change of the variable (8) in (7), the equation was converted to the following form (9).

$$-Q_0\omega^2 e^{i(\omega t-\varphi)} + 2\alpha i\,\omega Q_0 e^{i(\omega t-\varphi)} + \omega_0^2 Q_0 e^{i(\omega t-\varphi)} = \frac{V_0}{L} e^{i(\omega t-\varphi)} \tag{9}$$

$$\left[-Q_0\omega^2 + 2\alpha\omega Q_0 i + Q_0\omega_0^2\right] e^{i(\omega t-\varphi)} = \frac{V_0}{L} e^{i(\omega t-\varphi)} \Rightarrow \tag{10}$$

$$\left|-Q_0\omega^2 + 2\alpha\omega Q_0 i + Q_0\omega_0^2\right| = \left|\frac{V_0}{L}\right| \Rightarrow \tag{11}$$

$$Q_0\sqrt{\left(\omega_0^2-\omega^2\right)^2 + \left(2\alpha\omega\right)^2} = \frac{V_0}{L} \Rightarrow \tag{12}$$

$$Q_0 = \frac{\frac{V_0}{L}}{\sqrt{\left(\omega_0^2-\omega^2\right)^2 + \left(2\alpha\omega\right)^2}} \tag{13}$$

$$I_{1P} = +\frac{dQ_{1P}}{dt} \Rightarrow I_{1P} = \frac{\frac{V_0}{L}}{\sqrt{\left(\frac{\omega_0}{\omega}-1\right)^2 + \left(2\alpha\right)^2}} \tag{14}$$

In order to obtain the phase difference, with the assumption $\zeta = \alpha/\omega_0$ the following vector equation can be written:

$$\varphi = \tan^{-1}\left(\frac{2\alpha\omega}{\omega_0^2-\omega^2}\right) \Rightarrow \tan\varphi = \frac{2\zeta\left(\frac{\omega}{\omega_0}\right)}{1-\left(\frac{\omega}{\omega_0}\right)^2} \tag{15}$$

Given the result of the private response, the general response was also obtained.

$$I_{1h} = +\frac{dQ_{1h}}{dt} \tag{16}$$

$$L\frac{d^2Q_{1h}}{dt^2} + R\frac{dQ_{1h}}{dt} + \frac{Q_{1h}}{C} = 0 \Rightarrow \tag{17}$$

$$\frac{d^2Q_{1h}}{dt^2} + 2\alpha\frac{dQ_{1h}}{dt} + \omega_0^2\frac{Q_{1h}}{C} = 0 \tag{18}$$

Assuming $Q_{1h}(t) = Ke^{st}$, can be written:

$$s^2Ke^{st} + 2\alpha sKe^{st} + \omega_0^2Ke^{st} = 0 \Rightarrow \tag{19}$$

$$\left(s^2 + 2\alpha s + \omega_0^2\right)e^{st} = 0 \Rightarrow \tag{20}$$

$$s^2 + 2\alpha s + \omega_0^2 = 0 \Rightarrow \tag{21}$$

$$s = \frac{-2\alpha \pm \sqrt{(2\alpha)^2 - 4\omega_0^2}}{2} = -\alpha \pm \sqrt{\alpha^2 - \omega_0^2} \tag{22}$$

$$\text{if}: \ \zeta > 1 \Rightarrow Q_{1h}(t) = K_1e^{s_1t} + K_2e^{s_2t} \tag{23}$$

$$\text{if}: \ \zeta = 1 \Rightarrow Q_{1h}(t) = (K_1t + K_2)e^{s_1t} \tag{24}$$

$$\text{if}: \ \zeta < 1 \Rightarrow Q_{1h}(t) = K_1e^{-\alpha t}\cos(\omega_n t) + K_2e^{-\alpha t}\sin(\omega_n t) \tag{25}$$

$$\text{Then } \omega_n \text{ is } \omega_n = \sqrt{\omega_0^2 - \alpha^2}. \tag{26}$$

Given the general response and the private response of (5), The final answer is as following:

$$I_1 = I_{1h} + I_{1P} \tag{27}$$

The second part is related to the negative signal part, and its range is from π/ω to $2\pi/\omega$. Due to the use of the diode in the circuit to store the positive signal part and Lack of the requirement to store the negative part, so in this section, a homogeneous equation is obtained that equals to the response of (17). The initial conditions in this section according to (30) was used to calculate the constants.

$$\text{Second: } \frac{\pi}{\omega} \le t \le \frac{2\pi}{\omega} \tag{28}$$

$$L_g\dot{I}_2 + R_gI_2 + \frac{1}{C}\int I_2dt = 0 \Rightarrow I_2 = I_{1h} \tag{29}$$

$$\text{Initial Condition}: I_1\left(\frac{\pi}{\omega}\right) = I_2\left(\frac{\pi}{\omega}\right),\ \dot{I}_1\left(\frac{\pi}{\omega}\right) = \dot{I}_2\left(\frac{\pi}{\omega}\right) \quad \text{Whereas } I_2 \ge 0 \tag{30}$$

where L_g, R_g, C and I are, the inductance, electrical resistance, capacitance of the capacitor and current, respectively. Given that the generated voltage happened as sinusoidal half-cycle and is stored; Therefore, in the first section, the alternating voltage of the sinusoid was considered, and in the second part due to the lack of the voltage storage, the right side equal to zero.

Given the currents output in both parts, the voltage stored in the capacitor can be calculated from (31).

$$V_C = \frac{1}{C}\left(\int_0^{\frac{\pi}{\omega}} I_1dt + \int_{\frac{\pi}{\omega}}^{\frac{2\pi}{\omega}} I_2dt\right) \tag{31}$$

2.7 Designing the Safety Mechanism of MIG

In the design of the MIG, a safety mechanism has been used. This mechanism was designed to prevent activation of the MIG at accelerations below 500'g. This design includes a thin steel plate with a thickness of 0.2 mm. This plate by spot welding was attached to the end of the MIG housing. Due to the shear stress of the steel plate that extracted from the tensile test, as well as the mass and acceleration of the moving part of the MIG, using (32), the effective cross-sectional area of the plate, was obtained 2774mm^2.

$$\tau_{ts} = \frac{F}{A} \tag{32}$$

In which, τ is the shear stress in [Pa], F is the applied force to the shear plate in [N], and A is the effective cross-sectional area in [mm^2].

The design and numerical solution of this plate were carried out by the FEM so that after designing it in the Part module, The extracted mechanical properties of the tensile test were applied to it in the property module, then, in load module was allowed it to move vertically, while other degrees of freedom were equal to zero. Finally, after meshing the model, ABAQUS solved the problem.

3 Results and Discussion

3.1 Proposed Statistical Model and its Analysis

After analyzing the RSM-BBD proposals and obtaining their results in accordance with Table 2-II, a Second-order polynomial model for energy was extracted according to (33).

$$\begin{aligned}\text{Energy} = {} & 53.4 + 26.39D_c - 4.22H_m + 1.93H_d \\ & + 11.86H_h + 1.133T_L + 10.8T_w - 1.55D_cH_m \\ & + 1.2D_cH_c + 6.74D_cH_h + 2.6D_cT_L + 6.78D_cT_w \\ & - 3.47H_mH_d - 2.42H_mH_h + 0.025H_mT_L \\ & - 0.72H_mT_w - 2.16H_dH_h + 0.9H_dT_L + 1.22H_dT_w \\ & + 0.58H_hT_L + 3.74H_hT_w + 0.38T_LT_w + 2.75D_c^2 \\ & + 0.81H_m^2 + 0.96H_d^2 - 4.33H_h^2 - 3.82T_L^2 - 2.71T_w^2 \end{aligned} \tag{33}$$

The statistical analysis of the model presented in Table 3 is listed. Based on the results and statistical analysis, the Quadratic model is significant with P-value of less than 0.005, whereas its R^2 value is the highest value. Furthermore, the cubic model, although has high R^2, but, because of the P-value that is larger than the set value, so, the option has been undesirable.

The analysis of variance in the energy parameter was also presented in Table 4. The F-value for the model is 108.72 and there is less than 0.01% chance that this F-value is due to noise only. Moreover, in this model, the sentences Prob>F value less than 0.05, are important and significant. In the case, the sentences include: D_c, H_m, H_d, H_h, T_w, D_cH_h, D_cT_L, D_cT_w, H_mH_d, H_mH_h, H_dH_h, H_hT_w, H_h^2, T_L^2, T_w^2, are significant. In the meanwhile, with respect to the F-value of the parameter D_c (core diameter), can be found that it has the greatest effect on the energy increase. In contrast, the parameter T_L (lid thickness) has the lowest possible effect on energy with the F-value Equals 3.52. Given the sum of squares value in Table 4, it can be extracted the effect of each parameter in terms of weight. The parameter D_c which has the highest F-value, having a 65.92% contribution on the energy level, and also the parameters H_m and T_w, which have an effect of 13.32% and 11.33%, respectively. Among other parameters, the parameter T_L has the lowest effect equal to ~ 0.11%. Furthermore, due to the effect of parameters interactions on energy, it can be pointed to D_cH_h, D_cT_w, and H_hT_wi, which have the highest effect on the energy with ~ 2.9%, ~ 1.44%,

Table 2 RSM-BBD proposals and their results from FEM.

	I						II
Run	D_c [mm]	H_m [mm]	H_d [mm]	H_h [mm]	T_L [mm]	T_w [mm]	Energy [mJ]
1	6	9	2	2	1	1	20.1
2	10	9	2	2	1	1	62.0
3	6	12	2	2	1	1	18.7
4	10	12	2	2	1	1	58.1
5	6	9	2	4	1	1	34.6
6	10	9	2	4	1	1	108.8
7	6	12	2	4	1	1	27.2
8	10	12	2	4	1	1	91.5
9	8	9	1.5	3	0.5	1	51.8
10	8	12	1.5	3	0.5	1	47.5
11	8	9	2.5	3	0.5	1	60.8
12	8	12	2.5	3	0.5	1	45.7
13	8	9	1.5	3	1.5	1	46.7
14	8	12	1.5	3	1.5	1	48.6
15	8	9	2.5	3	1.5	1	62.4
16	8	12	2.5	3	1.5	1	47.3
17	8	10.5	1.5	2	1	0.5	26.8
18	8	10.5	2.5	2	1	0.5	31.4
19	8	10.5	1.5	4	1	0.5	45.7
20	8	10.5	2.5	4	1	0.5	40.0
21	8	10.5	1.5	2	1	1.5	40.1
22	8	10.5	2.5	2	1	1.5	48.5
23	8	10.5	1.5	4	1	1.5	72.3
24	8	10.5	2.5	4	1	1.5	73.7
25	6	10.5	2	2	0.5	1	18.8
26	10	10.5	2	2	0.5	1	49.2
27	6	10.5	2	4	0.5	1	30.5
28	10	10.5	2	4	0.5	1	83.5
29	6	10.5	2	2	1.5	1	18.8
30	10	10.5	2	2	1.5	1	56.9
31	6	10.5	2	4	1.5	1	30.1
32	10	10.5	2	4	1.5	1	96.2
33	8	9	2	3	0.5	0.5	41.6
34	8	12	2	3	0.5	0.5	32.5
35	8	9	2	3	1.5	0.5	41.9
36	8	12	2	3	1.5	0.5	34.6
37	8	9	2	3	0.5	1.5	60.0
38	8	12	2	3	0.5	1.5	52.7
39	8	9	2	3	1.5	1.5	66.5
40	8	12	2	3	1.5	1.5	51.6
41	6	10.5	1.5	3	1	0.5	21.4
42	10	10.5	1.5	3	1	0.5	63.5
43	6	10.5	2.5	3	1	0.5	22.4
44	10	10.5	2.5	3	1	0.5	66.2
45	6	10.5	1.5	3	1	1.5	29.3
46	10	10.5	1.5	3	1	1.5	95.4
47	6	10.5	2.5	3	1	1.5	31.5
48	10	10.5	2.5	3	1	1.5	105.5
49	8	10.5	2	3	1	1	54.0
50	8	10.5	2	3	1	1	52.8
51	8	10.5	2	3	1	1	54.0
52	8	10.5	2	3	1	1	52.8
53	8	10.5	2	3	1	1	54.0
54	8	10.5	2	3	1	1	52.8

Table 3 Statistics of the surface energy model.

Source	Lack of fit p-value	Adjusted R^2	Predicted R^2	Remark
Inertia	< 0.0001	0.9055	0.8864	–
2FI	0.0002	0.9590	0.9209	–
Quadratic	0.0011	0.9821	0.9544	Suggested
Cubic	0.0173	0.9963	0.8793	Aliased

Table 4 Variance analysis of the energy response model.

Source	Coefficient estimate	Sum of squares	df	Mean square	F-value	P-value prob > F	Remark
Model	–	25355.56	27	939.09	108.72	< 0.0001	significant
D_c	26.39	16716.48	1	16716.48	1935.21	< 0.0001	significant
H_m	-4.22	426.73	1	426.73	49.40	< 0.0001	significant
H_d	1.93	89.32	1	89.32	10.34	0.0035	significant
H_h	11.86	3377.25	1	3377.25	390.97	< 0.0001	significant
T_L	1.13	30.38	1	30.38	3.52	0.0720	
T_w	10.80	2797.20	1	2797.20	323.82	< 0.0001	significant
D_cH_m	-1.55	19.22	1	19.22	2.23	0.1478	
D_cH_c	1.20	11.52	1	11.52	1.33	0.2587	
D_cH_h	6.74	726.30	1	726.30	84.08	< 0.0001	significant
D_cT_L	2.60	54.08	1	54.08	6.26	0.0190	
D_cT_w	6.78	367.21	1	367.21	42.51	< 0.0001	significant
H_mH_d	-3.47	96.61	1	96.61	11.18	0.0025	significant
H_mH_h	-2.42	47.05	1	47.05	5.45	0.0276	
H_mT_L	0.025	0.010	1	0.010	1.158E-003	0.9731	
H_mT_w	-0.72	4.21	1	4.21	0.49	0.4916	
H_dH_h	-2.16	37.41	1	37.41	4.33	0.0474	
H_dT_L	0.90	6.48	1	6.48	0.75	0.3943	
H_dT_w	1.22	23.77	1	23.77	2.75	0.1092	
H_hT_L	0.58	2.65	1	2.65	0.31	0.5847	
H_hT_w	3.74	111.75	1	111.75	12.94	0.0013	significant
T_LT_w	0.38	1.13	1	1.13	0.13	0.7211	
D_c^2	2.75	77.94	1	77.94	9.02	0.0058	significant
H_m^2	0.81	6.70	1	6.70	0.78	0.3866	
H_d^2	0.96	9.50	1	9.50	1.10	0.3039	
H_h^2	-4.33	193.27	1	193.27	22.37	< 0.0001	significant
T_L^2	-3.82	149.94	1	149.94	17.36	0.0003	significant
T_w^2	-2.71	75.76	1	75.76	8.77	0.0065	significant
Residual		224.59	26	8.64			
Lack of Fit		222.43	21	10.59	24.52	0.0011	significant
Pure Error		2.16	5	0.43			
Cor Total		25580.15	53				
Std. Dev.			2.94		R-squared	0.9912	
Mean			50.58		Adj R-squared	0.9821	
C.V. %			5.81		Pred R-squared	0.9544	
PRESS			1165.19		Adeq precision	43.175	
-2 Log likelihood			230.21		BIC	341.90	AICc 351.17

~ 0.4%, whereas the remaining weight percent is ~ 0.88%. The desirability of the model was also evaluated by different standards: F-value for the Lack of fit was 24.52, which is significant, whereas there is a 0.11% chance that this F-value is due to noise only. The pred. R^2 and adj. R^2 quantities are 95.44% and 98.21%, respectively, which is a difference of less than 2%; this Percentage difference showed the results were reasonable. Adeq precision, which represents the signal-to-noise ratio, for this model was 43.175. With the determination of the number 4 as the standard value for this quantity and 43.175 value that is larger than the standard value, it can be concluded that the signal-to-noise ratio is significant. Therefore, it can be said the proposed model can be used as an optimum design.

In the presented optimum design, the goal is to maximize energy. To fitting it; the Optimum value of other parameters of the MIG should be achieved within the specified range. In addition to the range, and the 'Weight Value', the degree of 'importance' was also applied to each of the parameters. By determining the 'Desirability Function' (D) that affects the Maximization, the optimum level of the six parameters and the resulting energy is closer to reality. Whereas the degree of significance can change the optimum response, in this design, according to Table 5, 'importance' 3(+++) was given to all parameters and 5(+++++) was assigned to Energy. The 'Desirability Function' (Eq. (34)) was introduced by Myers and Montgomery [25]. The 'Desirability Function' is an objective function that contains two parameters; desirable value (di) which changes from 0 to 1, and weights & importance (r_i). The 'Desirability Function' was calculated from (34) and (35).

$$D = \left(d_1^{r_1} \times d_2^{r_2} \times \ldots \times d_n^{r_n}\right)^{\frac{1}{\sum r_i}} = \left(\prod_{i=1}^{n} d_i^{r_i}\right)^{\frac{1}{\sum r_i}} \tag{34}$$

$$\begin{cases} d_i = 0 & \text{Response}_i \le \text{Low}_i \\ d_i = 1 & \text{Low}_i < \text{Response}_i < \text{High}_i \\ d_i = 0 & \text{Response}_i \ge \text{High}_i \end{cases} \tag{35}$$

Table 5 Constraint of the optimization.

Name	Goal	Lower limit	Upper limit	Lower weight	Upper weight	Importance
D_c	is in range	6	10	1	1	3
H_m	is in range	9	12	1	1	3
H_d	is in range	1.5	2.5	1	1	3
H_h	is in range	2	4	1	1	3
T_L	is in range	0.5	1.5	1	1	3
T_w	is in range	0.5	1.5	1	1	3
Energy	maximize	18.7	108.8	1	1	5

Table 6 obtained optimum levels from the RSM-BBD.

Parameters	D_c	H_m	H_d	H_h	T_L	T_w	Energy prediction
Value	10 mm	4 mm	2.5 mm	9 mm	1 mm	1.5 mm	131/7 mJ

(a) (b)

Fig. 6 Schematic of the MIG: a) 2D mode, and b) MIG.

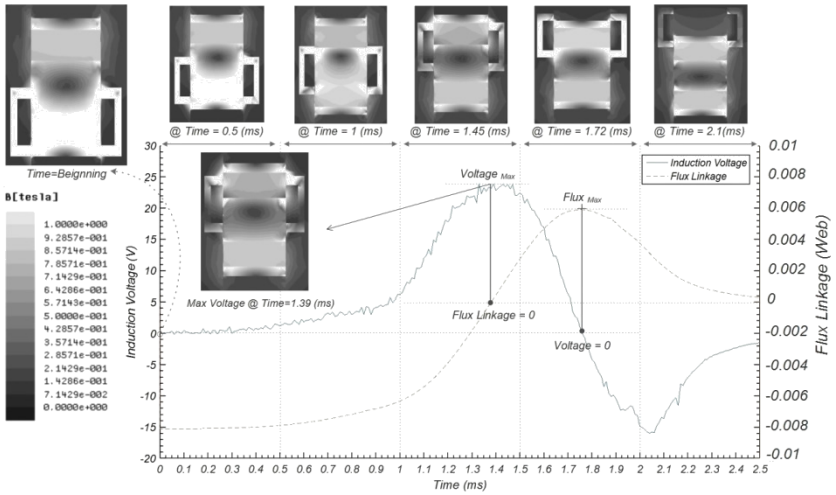

Fig. 7 The produced voltage and flux diagrams of the optimum model in the numerical solution.

According to the results of RSM-BBD, the optimum levels of the parameters were listed in Table 6. Some of the parameters, due to the limitation in manufacturing, were rounded to the nearest selective levels (Table 1).

3.2 Result of Optimum Numerical solution and its Analysis

After the optimum dimensions were obtained by RSM-BBD as listed in Table 6, the MIG was designed in the ANSYS Maxwell simulation program and simulated according to Section 2.5, also the designed optimum model is visible in Fig. 6.

Optimized bobbin include; the number of coil=100, diameter= 0.2mm, resistance and inductance are 2Ω, 0.41mH, respectively. Furthermore, the obtained result from the numerical solution is given in Fig. 7.

At the beginning of the core movement inside the coil, as shown in Fig. 7, the large part of the lower permanent magnet flux indirectly enters the housing through the iron lower disk. With passed time, after the iron disc is pulled out of the magnetic circuit, The lower permanent magnet flux, directly and with more quickly enter the housing, its field contour in Time = 0.5ms is obvious. In the second phase, whereas the lower permanent magnet is exiting the magnetic circuit, upper permanent magnet is at the threshold of entering the magnetic circuit (Time = 1ms). It can be seen that the amount of the magnetic flux due to the output of the lower permanent magnet has been reduced. In the third phase, not only, with the exiting of the lower permanent magnet, the

amount of the magnetic flux be decreased, but also by the entering of the permanent magnet to the magnetic circuit, the direction of flux, changes. By increasing the flux from the upper permanent magnet and its entering into the housing, in a specified moment, incoming flux equals to the amount of magnetic flux remaining from the lower permanent magnet. So the flux becomes zero, whereas flux Fluctuation at the specified moment, is maximum. According to the Faraday induction law (Eq. (36)), which is a function to magnetic flux variations and not the magnetic flux, the highest voltage is generated in Time = 1.39ms, whose flux is zero. In the fourth phase, with the full placement of the upper permanent magnet in the magnetic circuit, the maximum magnetic flux is directly entered into the housing, so, the magnetic flux curve arrives at the maximum value. In the fifth phase, due to the entering-indirect of magnetic flux through the iron upper disc, the magnetic flux is decreased. This Decrease of magnetic flux is faster due to air placement in the magnetic circuit (Time = 2.1ms), which has a lower permeability than other core parts. Due to the Faraday induction law, the output voltage is a function of the flux linkage (X). The formulation of Faraday's induction law is given in (36).

$$V_0 = -\frac{dX}{dt} = -\frac{dX}{dx}\frac{dx}{dt} = -\frac{dX}{dx}v \tag{36}$$

This relationship shows that whatever the Process is faster; the voltage will be higher. On the other hand, due to the acceleration stable during the production of the voltage, the velocity is a function of time. According to (36), experiments were carried out at various accelerations to determine the effect of acceleration on energy. These experiments were carried out with the optimum dimensions of RSM-BBD, which are described in Table 7 and Figs. 8 and 9.

It can be seen that in Fig. 8, with increasing acceleration, the produced voltage increases in accordance with (36), whereas this increases is true for the produced power as shown in Fig. 9, but it is not true for energy. By calculating the surface under the power-time curve that represents energy, energy is obtained. After calculating the energy through Fig 9 that is expressed in Table 7, it was found that increasing acceleration, it does not always increase energy. Furthermore, every generator with different dimensions, under a certain acceleration, will experience the maximum energy.

3.3 Experimental Validation of the Numerical Results

According to the required characteristics of the optimum MIG in Table 8, after extracting the MIG parts optimum geometry, the parts were manufactured and assembled (Fig. 10). For testing, given that the MIG experiences an acceleration of 800'g, so, a fixture was made to fix it during the test. After that, the MIG was placed in the fixture, and it connected to the shock test system.

For the experimental validation, due to the activation of the MIG under initial acceleration, the mechanical shock test system (Fig. 11) was selected. The test system consists of two-part, the stationary base and the movable part, that the MIG connects to the movable part, and then it must be positioned at a certain height (from zero-level, here stationary base considered as zero-level) and finally drop. The MIG, in this process, experiences a free drop until it hit the stationary base

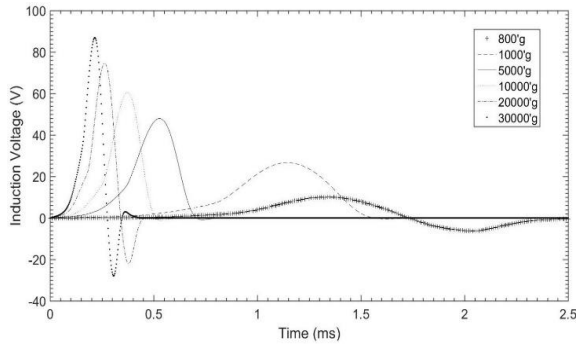

Fig. 8 Produced voltage at different accelerations.

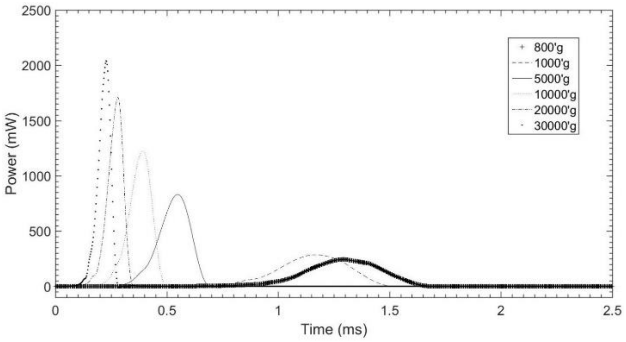

Fig. 9 Produced power at different accelerations.

Table 7 Extracted results of the MIG at different accelerations.

Row	Voltage [V]	Current [A]	Frequency [Hz]	Initial acceleration [m/s^2]	Energy [mJ]
1	25	13.1	350	800'g	139.9
2	28.2	14.8	400	1,000'g	162
3	50.7	17.8	715	5,000'g	268
4	63.3	21.1	840	10,000'g	398
5	76.4	23.5	1670	20,000'g	146
6	88	24.8	2500	30,000'g	133

Table 8 Required characteristics for projectile fuse.

Row	Item	Specification
1	Diameter	≤ 16 mm
2	Height	≤ 20 mm
3	Weight	≤ 20 gr
4	Charging voltage @ 100μF	≤ 12 V
5	Charging time @ 100μF	≤ 2 msec
6	Critical acceleration for operation	≤ 500'g

(zero-level). After the collision, the movable part will upwards according to Newton's third law. During the hit, and then rising up the moveable part that occurs within a few milliseconds, the movable part will be experiencing (as well as the MIG) the initial acceleration. In this study, acceleration needs to be 800'g, so after some testing, the desired height for the desired acceleration was found. However, to saw the acceleration, an accelerometer was installed on the movable part (adjacent to the generator). Fig. 12. shows the capacitor charging signal, which indicates a capacitor of 100μF within 1.1ms, was charged. Fig. 13 also illustrates the comparison between capacitor charging in two numerical and experimental methods, which shows, there is 10% error in the voltage storage and about 5% in the charging time of the capacitor.

3.4 Validation of Numerical and Analytical Results of MIG Safety Mechanism

Due to the numerical solution, it was observed that the result was extracted from the numerical solution conformed to its Analytical solution. Therefore, this mechanism can keep safe the MIG from unwanted mechanical shocks. Additionally, images of the plate cutting in Fig. 14. also shown.

3.5. Discussion on the results

The 3D figures of the presented response level by the second-order regression model were extracted from (33), which can be used to analyze the effect of each independent parameter on the energy level. Fig. 15. is shown the interaction between the two parameters, the magnet diameter and the magnet height, that effect on the energy level. According to Fig. 15, whereas other parameters were assumed to be constant in themselves optimum level, it is determined that whatever the height and diameter parameters of the magnet increases, the produced energy will also increase. By determining the magnet diameter = 10mm

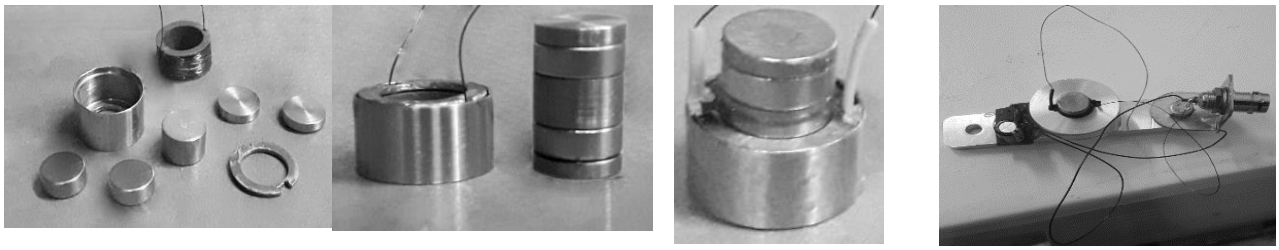

(a) (b) (c) (d)

Fig. 10 Parts of the MIG with the fixture such that a): parts of the MIG in the separate form, b): assembling the fixed and moving parts of the MIG, c): complete installation of the MIG along with the signal transducer, and d): complete assembly.

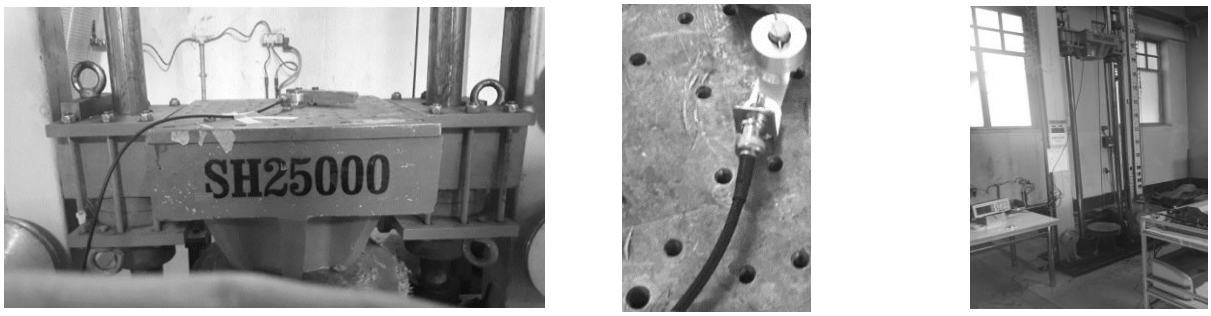

(a) (b) (c)

Fig. 11 Shock test system with the assembly of the miniaturized inertia generator (MIG) on it.

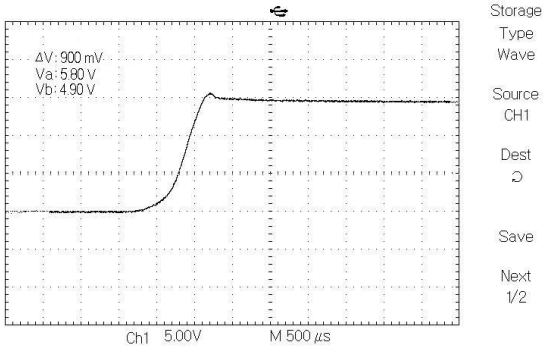

Fig. 12 The capacitor charging signal of the MIG.

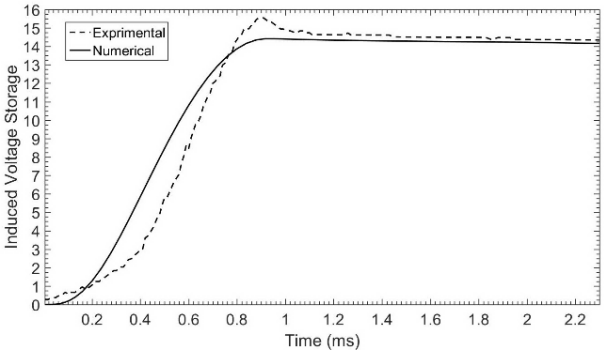

Fig. 13 Comparison of charged capacitors in numerical and experimental methods.

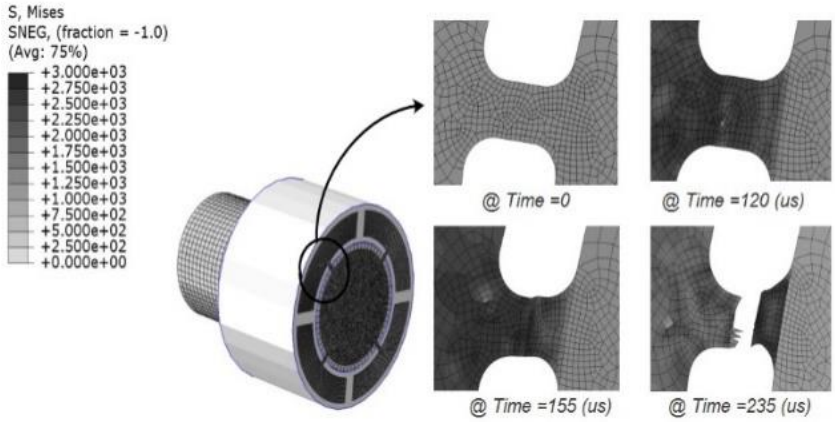

Fig. 14 The plate cutting at process different times.

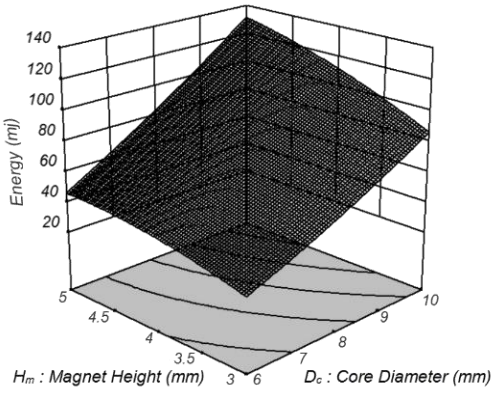

Fig. 15 The interaction between the two parameters, magnet diameter, and magnet height.

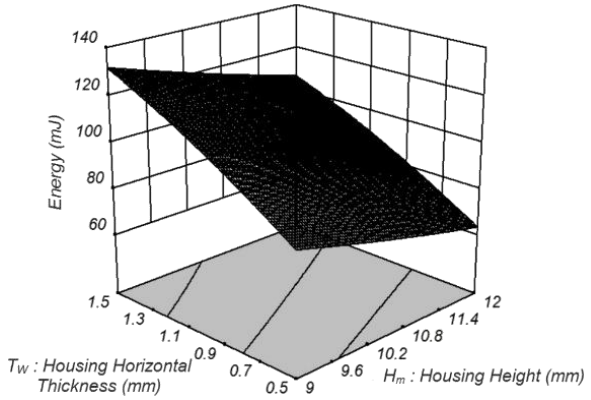

Fig. 16 The interaction between the two parameters the housing height and the housing horizontal thickness

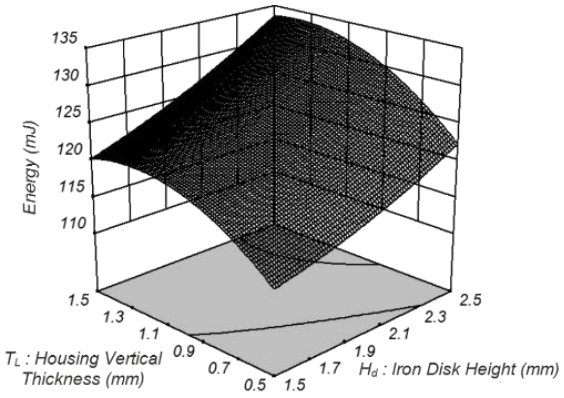

Fig. 17 The interaction between the two parameters the iron discs height and the housing vertical thickness.

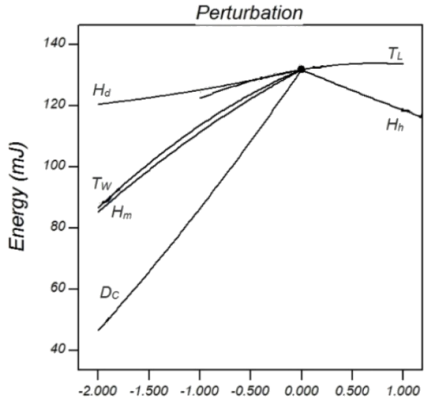

Fig. 18 The effect of the six parameters of the MIG on produced energy.

and the height = 4mm, as shown, the maximum amount of energy reached 131.7mJ.

In Fig. 17, the effect of the core discs and the vertical (lid) thickness of the housing on the energy level was investigated. With regards to the curved surface of Fig. 17, it can be concluded that the two parameters were less effective than the other parameters, and, respectively, with a value of 2.5mm and 1mm, can produce the maximum energy.

Fig. 18. shows the effect of six parameters on the energy level. As seen on, the greater slope of each parameter, have a greater effect on the energy level.

Fig. 19(a) shows the residual analytical diagram of the energy level. Whereas in this diagram, the remainders should follow a normal distribution like a line, the diagram shows that the remaining points, to exception a few points, all are on a line. On the other hand, in Fig. 19(b), a comparison shown between the real, and

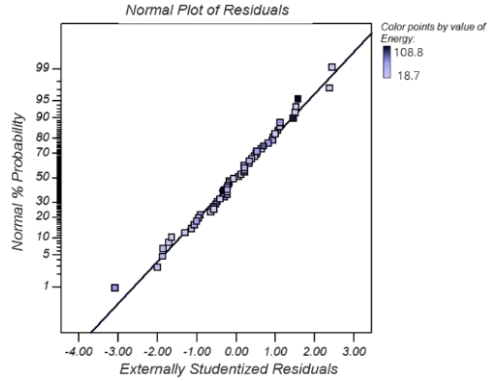

(a)

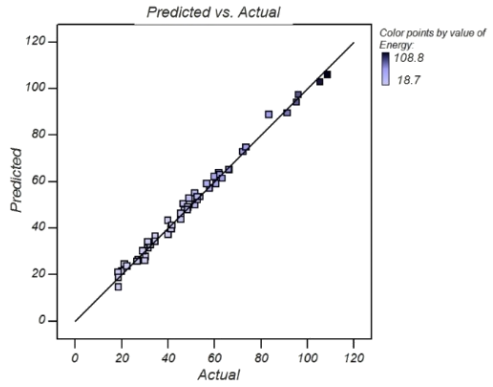

(b)

Fig. 19 Analytical figures of the produced energy model.

predict results. Noticeably, there is a good correlation between the mentioned results that $R^2 = 0.9912$ confirmed this.

4 Conclusion

In this paper, using RSM, the geometric parameters of a MIG were extracted to generate maximum energy, which was designed by BBD and analyzed by ANOVA. The analysis of the six parameters shown that;

- The diameter and height of the magnet are the most influential parameters on the energy so that, with increasing from 6mm to 10mm and 9mm to 12mm respectively; the generated energy from the amount of 30mJ with a rise of 450% arrives in 131.7mJ (Fig. 15).
- The housing vertical (wall) thickness and the iron discs height used in the core, are the parameters that the lowest effect on the produced energy So that their increase or decrease does not have a significant effect on produced energy Also, the energy range rises from 118 mJ to 131.7mJ that interacting efficiency increases to 10%. Furthermore, their optimum values are determined proportionally to the dimensions of the MIG (Fig. 17).
- The housing height, whereas the height of the core is fixed, has an inverse relationship with the increase in energy level. so that, decrease in height from 12mm to 9mm, leads to an increase in energy from 60mJ to 131.7mJ. Furthermore, increases productivity by up to 200% (Fig. 16).
- The housing horizontal thickness, as a magnetic flux passageway, has a direct relation with the increase in energy, which fits with different dimensions of the magnet, and it can take different values (Fig. 16).
- Although with Increase accelerates, the production of voltage and power also increases, but it is not true for energy, and the acceleration should be found proportional to the energy maximization (Figs. 8 and 9).

In addition to the analysis, verification performed between the numerical and experimental results and showed that there is a 5% error -in the charge capacity. Finally, this research showed that the proposed design not only increases the efficiency of the MIG but also specifies the effect of each parameter on the energy level.

References

[1] P. Glynne-Jones, M. J. Tudor, S. P. Beeby, and N. M. White, "An electromagnetic, vibration-powered generator for intelligent sensor system," *Sensors and Actuators A*, Vol. 110, No. 1, pp. 344–349, 2004.

[2] C. B. Williams and R. B. Yates, "Analysis of a micro-electric generator for microsystem," *Sensors and Actuators A*, Vol. 52, No. 2, pp. 8–11, 1996.

[3] J. B. Lee, Z. Chen, M. G. Allen, and A. Rohatgi, "A miniaturized high-voltage solar cell array as an electrostatic MEMS power supply," *Journal of Micromechanical Systems*, Vol. 4, No. 3, pp. 102–108, 1995.

[4] H. Hoppe and N. S. Sariciftci, "Organic solar cells," *Journal of Materials Research*, Vol. 19, No. 7, pp. 1924–1945, 2004.

[5] T. Matsui, H. Sai, T. Suezaki, M. Matsumoto, K. Saito, I. Yoshida, and M. Kondo, "Development of highly stable and efficient amorphous silicon based solar cells," in *28th European Photovoltaic Solar Energy Conference and Exhibition*, pp. 2213-2217, 2013.

[6] M. Z. Iqbal and A. U. Rehman, "Recent progress in graphene incorporated solar cell devices," *Solar Energy*, Vol. 169, pp. 634–647, 2018.

[7] B. O'regan and M. Grfitzeli, "A low-cost, high-efficiency solar cell based on dye-sensitized," *Nature*, Vol. 353, pp. 737–740, 1991.

[8] J. G. Radich, R. Dwyer, and P. V. Kamat, "Cu_2S reduced graphene oxide composite for high-efficiency quantum dot solar cells. Overcoming the redox limitations of S_2^-/S_n^{2-} at the counter electrode," *Journal of Physical Chemistry Letters*, Vol. 2, No. 19, pp. 2453–2460, 2011.

[9] Z. L. Wang, "On Maxwell's displacement current for energy and sensors: the origin of nanogenerators," *Materials Today*, Vol. 20, No. 2, pp. 74–82, 2017.

[10] P. P. Alves, "A experiência de joule revisitada," *M.Sc. Thesis*, Universidade Nova de Lisboa, Lisboa, 2008.

[11] D. Champier, "Thermoelectric generators: A review of applications," *Energy Conversion and Management*, Vol. 140, pp. 167–181, 2017.

[12] Z. H. Zheng, P. Fan, J. T. Luo, G. X. Liang, and D. P. Zhang, "Enhanced thermoelectric properties of antimony telluride thin films with preferred orientation prepared by sputtering a fan-shaped binary composite target, " *Journal of Electronic Materials*, Vol. 42, No. 12, pp. 3421–3425, 2013.

[13] M. B. Thomas, "Thermoelectric energy harvesting in small-caliber projectiles," in *Technical Digest PowerMEMS*, pp. 261–264, 2009.

[14] J. M. Seo, H. S. Lim, J. Y. Park, M. R. Park, and B. S. Choi, "Development and experimental investigation of a 500-W class ultramicro gas turbine power generator," *Energy*, Vol. 124, pp. 9–18, 2017.

[15] S. H. Yoon, J. T. Son, and J. S. Oh, "Miniaturized g- and spin-activated $Pb/HBF_4/PbO_2$ reserve batteries as power sources for electronic fuzes," *Journal of Power Sources*, Vol. 162, No. 2, pp. 1421–1430, 2006.

[16] C. C. Enz, A. El-Hoiydi, J. D. Decotignie, and V. Peiris, "WiseNET: An ultralow-power wireless sensor network solution, " *IEEE Computer Society*, Vol. 37, No. 8, pp. 62–70, 2004.

[17] S. Roundy, P. K. Wright, and J. Rabaey, "A study of low level vibrations as a power source for wireless sensor nodes, " *Computer Communication*, Vol. 26, No. 11, pp. 1131–1141, 2003.

[18] S. Roundy and P. K. Wright, "A piezoelectric vibration based generator for wireless electronics," *Smart Materials and Structures*, Vol. 13, pp.1131–1142, 2004.

[19] C. E. Buzzell and R. T. Ziemba, "Electrical setback generator," *US Patent 3 981 245*, Dec. 1976.

[20] J. Wang, W. Wang, G. W. Jewell, and D. Howe, "A low-power, inertia, permanent-magnet generator/energy storage system," *IEEE Transaction on Industrial Electronic*, Vol. 49, No. 3, pp. 640–648, 2002.

[21] Y. Fu, W. Lou, and L. Zhang, "The simulation for a new nanomagnetic setback generator," in *Proceedings of the Institution of Mechanical Engineers, Part N: Journal of Nanoengineering and Nanosystems*, Vol. 225, No. 4, pp.177–180, 2012.

[22] O. Farrok, Md. Rabiul Islam, Y. Guo, J. Zhu, and W. Xu, "A novel design procedure for designing inertia generators," *IEEE Transaction on Industrial Electronic*, Vol. 65, No. 2, pp. 1846–1854, 2018.

[23] Q. Lu, L. Li, and G. Yin, "Optimization design of setback generator for initiating explosive devices," in *MATEC Web of Conferences*, Vol. 100, pp. 1–5, 2017.

[24] S. H. Yoon, J. S. Oh, Y. H. Lee, and S. W. Lee, "Miniaturized inertia generators as power supplies for small-caliber fuzes," *IEEE Transaction on Magnetics*, Vol. 41, No. 7, pp. 2300–2306, 2005.

[25] R. H. Myers, D. C. Montgomery, C. M. Anderson-Cook. *Response surface methodology: Process and product optimization using designed experiments*, John Wiley & Sons, 2016.

A. Rajabi was born in Tehran, Iran, August 23rd, 1992. He received his B.Sc. degree in Mechanical Engineering from Islamic Azad University (IAU) and also, M.Sc. degree in Mechanical Engineering-applied mechanics from Malek-Ashtar University of Technology (MUT), Tehran, Iran, in 2015 and 2018, respectively. His research interests involve on electromechanical systems design and renewable energy technologies.

H. Lexian was born in Neyshabur, Iran, April 27th 1978. He received the B.S. degree from the Department of Mechanical Engineering, Malek-Ashtar University of Technology (MUT), Isfahan, Iran, in 2001, the M.Sc. and the Ph.D. degrees in Mechanical Engineering from Amirkabir University of Technology (Tehran Polytechnic) in 2003 and 2009, respectively. He is currently an Assistant Professor in the Faculty of Material & Manufacturing Technologies, Malek Ashtar University of Technology (MUT), Iran. His research interests include stress analysis and system dynamic.